



Full-field characterisation of oxide-oxide ceramic-matrix composites using X-ray computed micro-tomography and digital volume correlation under load at high temperatures

J. Paul Forna-Kreutzer ^{a,b}, Jon Ell ^c, Harold Barnard ^d, Talha J. Pirzada ^{e,f}, Robert O. Ritchie ^c, Dong Liu ^{b,*}

^a Bristol Composites Institute (AC CIS), University of Bristol, Bristol, UK

^b School of Physics, University of Bristol, Bristol, UK

^c Department of Materials Science and Engineering, University of California, Berkeley, CA, USA

^d Advanced Light Source, Lawrence Berkeley National Laboratory, Berkeley, CA, USA

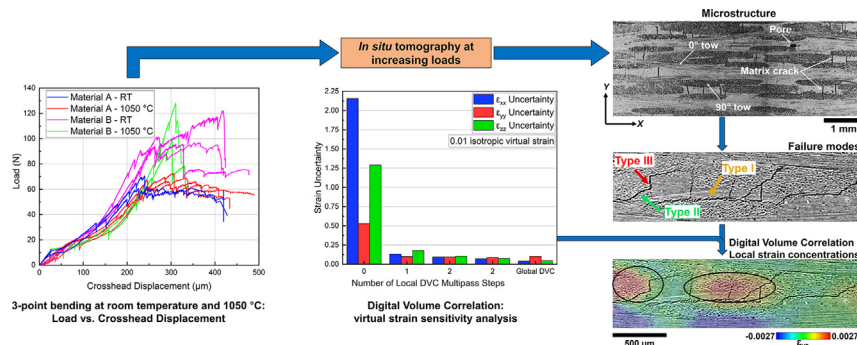
^e Cross Manufacturing Company, Bath, UK

^f Department of Materials, University of Oxford, UK

HIGHLIGHTS

- Higher sintering temperatures resulted in higher flexural failure strengths.
- Failure occurred through three primary cracking mechanisms in both materials.
- Pre-failure maximum principal strains were good predictors for fracture initiation.
- 3-D local microstructural strains revealed abrupt shear strain gradients.

GRAPHICAL ABSTRACT



ARTICLE INFO

Article history:

Received 22 March 2021

Revised 8 June 2021

Accepted 10 June 2021

Available online 11 June 2021

Keywords:

Oxide-oxide ceramic-matrix composites
In situ full-field characterisation
High-temperature X-ray computed micro-tomography
Digital volume correlation
Deformation and fracture

ABSTRACT

In situ synchrotron X-ray computed micro-tomography and digital volume correlation (DVC) were utilised to understand the failure mechanisms at room temperature and 1050 °C of two Nextel™720/alumina oxide-oxide ceramic-matrix composites (CMCs), termed materials A and B, sintered respectively at 1200 °C and ~1250 °C. At both test temperatures, three-point-bending strengths were ~55–58 MPa for material A and ~94–100 MPa for material B. Damage was associated with three primary types of cracking modes: interfacial delamination, inclined cracks within fibre tows, opening of existing matrix shrinkage cracks. Material A exhibited higher shrinkage cracking, whereas material B displayed more pronounced diagonal matrix microcracking. At 1050 °C, both systems showed less microcracking but more pronounced delamination. Such damage characteristics were rationalised in terms of the corresponding 3D DVC displacement/strain fields. Specifically, global DVC was utilised and maximum principal strain locations prior to failure, which varied from 0.005 to 0.01, correlated well to the fracture initiation sites. Further, abrupt positive to negative transitions of shear strain components were observed and were attributed to the different bonding strengths between 0°/90° fibres and the matrix. The current study demonstrates that *in situ* high-temperature tomography/DVC is a powerful method for studying the deformation and fracture of oxide-oxide CMCs.

© 2021 The Authors. Published by Elsevier Ltd. This is an open access article under the CC BY license (<http://creativecommons.org/licenses/by/4.0/>).

* Corresponding author.

E-mail address: dong.liu@bristol.ac.uk (D. Liu).

1. Introduction

Due to their superior toughness compared to monolithic ceramics, lower specific densities and better high-temperature performance than currently employed alloys, ceramic-matrix composites (CMC) represent a great potential for use in harsh environments such as those required by aerospace power generation systems, gas turbines and nuclear reactors [1,2]. In the case of turbine engines, the deployment of CMCs as turbine blades, vanes, seals or acoustic liners would enable reductions in both component mass and cooling requirements resulting in lower fuel consumption and gas emissions [3].

Historically, the majority of CMC research has focused on SiC fibre-based composites which has become a relatively mature and robust class of materials that has passed certification and entered service as certain non-rotating parts of turbofan engines [4]. Most often, SiC/SiC composites rely on fibre coatings to achieve improved toughness. Nonetheless, the volatilisation of the silica scale in the presence of water vapour can lead to increased material recession rates and oxidation at intermediate temperatures which ultimately limit the lifetimes of SiC/SiC composites in combustion environments [5,6].

To overcome these deficiencies, increasing attention has been given to oxide-oxide CMCs. This newer, less mature, class of materials offers great potential for long term use in oxidising environments despite their lower yield strength, weaker creep resistance and lower temperature capacity compared to SiC/SiC composites. Different from SiC-based CMCs, the fracture toughness in most advanced oxide CMC systems is achieved by a porous matrix which reduces fibre/matrix interfacial strength, thereby promoting crack deflection to avoid fibre failure [1,7,8]. This compliant matrix also acts as a propagation medium for cracks and lowers the stress concentrations at the fibre surface [9]. Thus, the total porosity of oxide CMCs is of prime importance for their efficient function with porosity values between 30 and 40% being regarded as optimal. Higher porosity renders the composite too weak whereas denser and stronger matrices lead to high stress concentrations imposed on the fibres [7]. Typically, two types of fibres have been adopted in oxide CMCs: 3M's Nextel™ 610 (>99% Al₂O₃) and Nextel™ 720 (N720: 85% Al₂O₃ – 15% SiO₂ weight ratio). The former offers superior strength whereas the latter has better creep resistance at high temperatures [9–12].

Due to the intended use of CMCs in harsh environments, there has been a recognised need to characterise such materials under conditions similar to service. For instance, Carelli et al. [13] found that the mechanical properties of a woven N720/mullite-alumina (fibre/matrix) composite depend on the testing orientation (0/90° or ±45°), and that the tensile strength and modulus can change dramatically after aging at 1200 °C for 1000 h. However, a similar tensile testing of N720/alumina (N720/A) specimens by Di Salvo et al. [14] showed an increase in failure strength at 1150 °C compared to 20 °C. The tensile fatigue and creep behaviour of woven N720/A composites have also been extensively investigated under a variety of conditions and been found to display a marked dependence both on temperature and gas atmosphere. Significant decreases in both properties were observed in air around 1200 °C with the addition of steam further deteriorating the mechanical properties of N720/A specimens. Loading rates also affect the material behaviour of woven 720/A CMCs with lower loading rates being associated with lower failure strengths but higher failure strains [15–19]. The objective of the present work is to focus on the flexural strength of two N720/A oxide-oxide CMCs at room temperature and 1050 °C in air and to relate the strength properties to a comprehensive three-dimensional quantitative evaluation of the evolution of damage under load at temperature in real time.

From previous studies it is readily apparent that to achieve a better understanding of the fracture behaviour of CMCs, such *in situ* characterisation is of utmost importance especially with the aim of improving the design of CMCs. The mere actions of unloading or cooling to ambient temperature can have a marked impact on residual stresses and hence on the fracture patterns which will not faithfully represent material behaviour. While most studies rely on two-dimensional imaging techniques such as scanning electron microscopy (SEM), attempts have been made to study CMCs using more advanced three-dimensional techniques such as X-ray computed microtomography (XCT) [20–24]. Due to the technical difficulty, *in situ* XCT under extreme conditions is even more scarce. Nevertheless, failure events in SiC CMCs were captured using synchrotron XCT at temperatures above 1650 °C by Bale et al. [25] in 2013 through the use of a unique hot cell and loading device. However, no further analysis of the 3D strain fields was conducted. In this work, we will combine *in situ* high-temperature synchrotron XCT with the digital volume correlation (DVC) method for a full-field characterisation of the deformation and fracture of N720/A CMCs.

DVC is an optical tracking technique initially reported as an 'extension to digital image correlation (DIC)': it utilises the inherent contrast of a material's microstructure in order to compute three-dimensional displacement and strain fields between sets of reference and deformed image stacks. The fundamental principle of DVC is based on that of optical flow conservation, *i.e.*, the passive transfer of the texture of a medium via a displacement field. As such, DVC enables the identification and quantification of local strain phenomena which may only be observable during *in situ* XCT testing and allows their correlation to the material's microstructure. Proposed by Bay et al. [26] in 1999 for use on trabecular bone, the method has since matured significantly, and exists nowadays under two main categories: *local* and *global* DVC. For local DVC, the region of interest is subdivided into subsets which are then independently correlated. Generally, only the displacement vector at the centre of each subset is kept and thus a post-processing step is required to generate a smooth displacement field. Conversely, in global DVC the computation is performed using all voxels of the entire region of interest at once to generate a continuous displacement field based on finite-element interpolation. A significant advantage of global DVC procedures is the generation of a residual field, *i.e.*, a set of images representing strictly the difference between the deformed dataset and the reference one. As such, areas where the displacement continuity is violated, by such scenarios as cracking, decohesion or noise patterns, will give rise to very visible features in the residual field, allowing detailed three-dimensional analyses of, for example, fracture mechanisms. An in-depth description of both local and global DVC can be found in the [Supplementary Materials](#) and in references [27–30].

While the most common application of the technique appears to be in the field of biomechanics, DVC has seen use in solid mechanics in the characterisation of *inter alia* nuclear graphite, fibre-reinforced polymers and lava-like fuel-containing materials [31–37]. Such materials provide sufficient microstructural contrast for the tracking of features at various length-scales. More importantly, owing to the heterogeneous microstructure of CMCs, consisting of fibres and matrix to generate a high degree of contrast and create an excellent medium for DVC, the method has also seen application with CMCs. Mazars et al. [38] performed high temperature *in situ* tensile testing of SiC/SiC CMCs and utilised global DVC for fracture investigation and strain quantification. Similarly, Saucedo-Mora et al. [39] applied local DVC to tension testing of braided SiC/SiC tubes for nuclear cladding applications. Furthermore, a recent study by Pirzada et al. [40] utilised local DVC to

investigate the fracture of oxide-oxide CMCs under bending. The study however lacks an in-depth sensitivity analysis on the application of DVC to oxide-oxide CMCs. Despite its obvious potential, there appears to be no published work on the application of global DVC on oxide CMCs especially under extreme conditions thus emphasising the novelty of the present study which aims to fill the current literature gap. Accordingly, in this work we systematically investigate both local and global DVC methods and apply these techniques, with high confidence through a detailed sensitivity analysis involving the identification and quantification of uncertainties and errors using repeat scans and virtually applied deformations, to *in situ* XCT images of oxide CMCs loaded in bending at ambient and high temperatures.

2. Experimental procedures

2.1. Materials

Investigated in the current study were two oxide-oxide CMC material systems produced by Composite Horizons LLC (PCC Structural) and supplied through Cross Manufacturing (Bath, UK). Both material systems consisted of N720 fibres (diameter 10–12 µm, 8-harness-satin weave, 0/90° orientation) and a porous alumina (Al_2O_3) matrix. The composites were fabricated through a slurry impregnation process whereby the dry fibre preform is impregnated by a slurry containing ceramic Al_2O_3 precursor powder particles to form matrix prepgres. The latter were subsequently stacked and consolidated through vacuum bagging at ~150 °C to remove water and any other remaining solvents. The final step of the manufacturing process, pressureless sintering, establishes the difference between the two tested systems. One material system, henceforth referred to as material A, was sintered at 1200 °C, whereas the second, material B was sintered at a temperature of approximately 1250 °C, with the exact temperature being proprietary to Composite Horizons. The sintered plates were then cut using a slow speed diamond saw (operating at 125 rpm) and were ground into rectangular beam specimens using SiC grinding paper in water. Extra care was taken to ensure that the 0° longitudinal fibre tows were aligned with the x-axis (span direction) of the three-point bend samples used for mechanical testing and the 90° transverse tows were parallel to the z-axis along the loading roller length (thickness direction), as per the axes defined in Fig. 1.

2.2. Experimental setup and digital volume correlation analysis

2.2.1. In situ mechanical testing with X-ray computed microtomography

In situ three-point bending tests with simultaneous synchrotron XCT imaging were carried out on beamline 8.3.2 at the Advanced Light Source in the U.S. Lawrence Berkeley National Laboratory. The unique environmental testing facility allows mechanical testing at elevated temperatures enabling the investigation of the CMCs under conditions that are relevant for service. A quick overview of the device will be given here; detailed descriptions of the set-up can be found in refs. [25,41]. The heating of the device was provided by six halogen lamps arranged in a configuration to create a uniform hot zone at the centre of the testing chamber. In the case of the bending experiments, the specimens were placed on two support rollers which were designed to fit directly in the middle of the hot zone created by the halogen lamps. To better understand the set-up and the determination of the uniformity of the hot zone, the reader is directed to ref. [40], in particular Fig. 5. The height of the sample was fitted within the 4 mm tall, 0.3 mm thick aluminium window which permits transmission of the incoming X-ray beam with low absorption. The temperature was measured using a thermocouple attached to the bottom surface of the bend specimens and was controlled through a programmable power supply [41]. The loading rollers were made of alumina and were 3 mm in diameter. Due to spatial restrictions inside the device chamber, a length/depth ratio of 7 was used, with classical beam theory was utilized to estimate the flexural strength of each sample according to ASTM Standard C1341 [42], viz.:

$$\sigma_U = \frac{3P_U L}{2BW^2}, \quad (1)$$

where σ_U is the flexural strength at maximum load (P_U), L is the loading span, W is the in-plane width and B is the out-of-plane thickness of the specimen. Specimen dimensions are presented in Table S1 in the [Supplementary Materials](#) and illustrated in Fig. 1 as a 2D representation.

During the experiments, beam samples were loaded monotonically to failure in an air atmosphere at room temperature (RT) and 1050 °C. *In situ* XCT scans were collected at different loading steps and were subsequently used for DVC analyses to derive the evolu-

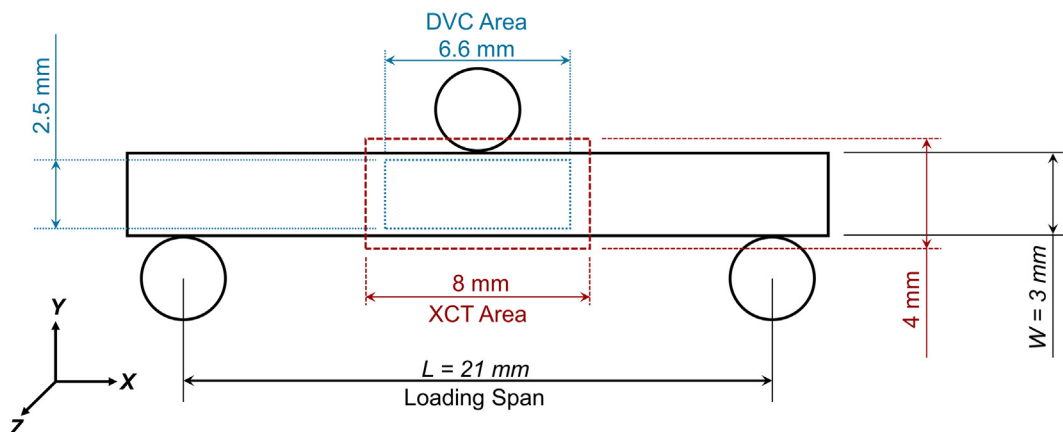


Fig. 1. Two-dimensional diagram of the three-point bending set-up and regions of tomographic acquisition and DVC analyses; Note: W is the in-plane width and B is the out-of-plane thickness of the specimen. The loading span (L)/ width (W) ratio is 7.

tion of 3D displacements and strains in the scanned volume. For the tomographic acquisition process, white light was used (6–43 keV) along with a PCO Edge 2 × CCD, 2560 × 2560 pixels camera as the detector. This configuration results in a pixel size of $3.25 \times 3.25 \mu\text{m}$ and a field of view of $8 \times 4 \text{ mm}$. For each scan, 1969 projections were acquired at 30 ms intervals over a 180° rotation with the acquisition time being $\sim 10 \text{ min}$. The reconstruction was conducted using a conventional Gridrec algorithm in the TomoPy software; the centre of rotation of each scan was individually identified to remove deformation artefacts. Flat field correction was applied to each scan as a measure to reduce detector fixed pattern noise.

The loading rig was operated under displacement control with the load applied by manual control of the loading roller in $\sim 1 \mu\text{m}$ increments per second. During each XCT scan the applied displacement was fixed and, as such, a certain level of load relaxation was observed. For each sample, a small pre-load of about 10 N was applied to avoid sample movement during scanning process. Successive scans were collected at 15–20 N loading steps. Depending on the failure load of each specimen, the total number of scans varied from three to nine. Scans were attempted directly before the predicted failure loads. Note that two XCT scans at the pre-load step were acquired for one specimen from each material system for DVC sensitivity analysis. Moreover, the nature of the three-point bending configuration dictated that the largest dimension of the specimen (*i.e.*, the length) was perpendicular to the axis of rotation which resulted in a small loss of microstructural detail which will be exemplified in the Results section. The scanning steps for all samples (annotated as material type-temperature-specimen number, *e.g.*, A-RT-1) are presented in Tables S2 and S3; the load at which the scans were collected was normalised by the peak load (P_U) for convenience.

2.2.2. Data processing and digital volume correlation

The reconstructed scans generated stacks of 32-bit tiff images which were processed in the open-source software ImageJ [43] prior to DVC. For each individual specimen, pre-alignment was applied to all the scans, ensuring that only the specimen (excluding air and loading rollers) was present in the field of view of the cropped dataset, as shown in the schematic in Fig. 1. A Gaussian blur filter (with a standard deviation of the Gaussian distribution of 1.0) was applied to reduce image noise; the contrast was adjusted to a fixed dynamic range of −1.1 to 2.4 and finally converted to 8-bit. These datasets were saved as raw data files and imported to the Avizo Lite - software version 2019.4 [44] for three-dimensional visualisation, manipulation and DVC. Every scan was down-sampled by a factor of 1.8 resulting in improved volume renderings and markedly faster computing. Using the *Image Registration* module in the Avizo ecosystem [44], all the scans of a single sample were aligned with the pre-load scan and were once more cropped to the exact same dimensions to ensure the best possible overlap.

DVC was used to generate local 3D displacement and strain maps at microstructural size-scales. Consequently, these are representative of the local strain distributions in the material as opposed to macroscopic global strains which refer to the specimen as a whole. The correlation quality was evaluated using a normalised cross-correlation coefficient and an average correlation residual which are described in more detail. The *XDigitalVolumeCorrelation* module present within the Avizo software [44] was used for both local and global DVC in this work. Note, in the context of DVC, the terms *local* and *global* refer strictly to the correlation method, not the scale of the strain distributions. Two methods were employed in the current work to determine the uncertainty of

the DVC analysis. Firstly, repeat scans were taken at the same pre-load state which were correlated to each other using both local and global DVC. In this case the accuracy was determined using the mean calculated strain value whereby positive and negative values cancel out (as these were repeat scans acquired at the same load, zero strain was expected). The second method involved the use of the *Transform* module available in Avizo to impose different known values of 3D ‘virtual strain’ on a single pre-load scan of material A (sample A-RT-1). The use of a single pre-load scan for this type of analysis was justified by the microstructures of all tested specimens being fundamentally identical as described in the Results section. Therefore, it was assumed that the results generated from the virtually deformed A-RT-1 specimen are applicable to every other specimen. Strains ranging from 0.0025 to 0.015 (0.0025 step-size) were applied to the datasets. The ensuing virtually deformed datasets were then correlated to the initial scans. The DVC methodologies for subsequent analysis of the datasets with applied known strains were as follows:

(i) *Local DVC*: utilised cubic sub-volume sizes of $31 \times 31 \times 31$ voxels (31^3). A multi-pass approach, as described in the [Supplementary Materials](#), was applied starting from sub-volumes of 53^3 voxels reaching the 31^3 size with decreasing step sizes of 22 (1-step multi-pass), 11 (2-step multi-pass) and 5.5 voxels (4-step multi-pass); a correlation threshold was set at 0.5 whereby for any subset whose correlation value was below this threshold, the displacement was calculated using an average of the neighbouring sub-volumes. The quality of correlation was evaluated using the normalised cross correlation coefficient $C_{\text{LA-DVC}}$:

$$C_{\text{LA-DVC}} = \frac{\sum f(X)g(X^*)}{\sqrt{\sum f(X)^2 \sum g(X^*)^2}}, \quad (2)$$

where X and X^* describe the voxel coordinates of the same location in the reference and deformed dataset and $f(X)$ and $g(X^*)$ refer to the scalar grey levels in the initial and deformed dataset. A value close to unity in this case represents perfect correlation [31].

(ii) *Global DVC*: utilised tetrahedral element sizes of 33 voxels initialised using the displacement field generated by the analogous 1-step and 4-step local DVC multi-pass computation; the number of iterations = 30; the convergence criterion = $0.001 \mu\text{m}$. The quality of correlation was evaluated using the average correlation residual, $R_{\text{GA-DVC}}$:

$$R_{\text{GA-DVC}} = \frac{\langle |r(x)| \rangle}{\max(f) - \min(f)}, \quad (3)$$

where $\langle |r(x)| \rangle$ is the average of $r(x) = f(X) - g(X^*)$ over the volume in interest and $\max(f)$ and $\min(f)$ are respectively the minimum and maximum grey levels within the reference dataset. For $R_{\text{GA-DVC}}$, a value of zero represents perfect correlation [30–31].

The uncertainty in normal strain (ε_{xx} , ε_{yy} , ε_{zz}) was quantified by dividing the standard deviation by the mean. The percent error was calculated by subtracting the imposed value from the DVC value, dividing by the imposed value and multiplying by 100; values are shown in the Results section. Based on the outcome of the uncertainty study, a modified 1-step local DVC was utilised to derive the 3D displacement and strain maps for the *in situ* scans. This consisted of a 1-step multi-pass, as described above for the first load step, while subsequent load steps were initialised using the displacement field from the preceding load step (*e.g.*, local DVC of load step n was initialised with the displacement field of load step $n-1$). Finally, the local DVC displacement was used to initialise the analogous global DVC with 33-voxel element sizes. An experimental flowchart summarising the experimental steps is included in Fig. S1.

3. Results

3.1. Microstructure of the two material systems

An overview of the microstructures of materials A and B is shown in Fig. 2a-b. As noted above, the nomenclature for naming the samples, *i.e.*, A-RT-1, refers to the material-test temperature-specimen number. Firstly, no systematic structural differences between the two material systems were observed. Therefore, the following observations refer to both materials A and B. The woven structure of the composites is clearly visible with a slightly reduced contrast in the 0° tows compared with 90° tows. Also visible are vertical matrix shrinkage cracks which are unevenly distributed both across different specimens and within the same specimen. More images are included in Fig. S2. More importantly, ubiquitous features of ‘tow splitting’ can be found in all tested specimens. These are visible in Fig. 2a and 2b; further, a 3D example of segmented fibre tows is shown in Fig. 2c and 2d. The latter two indicate three distinct groups of tows, *i.e.*, three separate ‘layers’ of 0° and 90° tows. Within each layer, the aforementioned ‘splitting’ of tows is visible. It is highly possible that instead of ‘splitting’, these sites represent the adjoining of different tows into a single one; nonetheless, this phenomenon will be referred to as ‘tow splitting’ in the present work. Such tow splitting was found to induce significant curvature within the tows and are, in certain areas of the specimens, associated with the formation of large pores, as shown in Fig. 2a and 2b and Fig. S2.

3.2. Mechanical testing

The load–displacement curves (RT and 1050 °C) of the two material systems are shown in Fig. 3a-b. The abscissa of the load–displacement diagrams in Fig. 3a-b represents the crosshead displacement; hence, a bedding-in stage at low loads is visible. The flexural strength data, derived using Eq. (1), are presented in Table 1. Despite the small number of specimens tested, which is due to the limited time commonly restricting synchrotron experiments, the strengths of specimens tested at the same temperatures

were consistent, *e.g.*, 57, 59 and 60 MPa for the three Material A specimens tested at RT. Overall, material B, with its somewhat higher sintering temperature, exhibited a higher mean strength; its strength was 60% larger than that of material A at room temperature and 88% larger at 1050 °C. Furthermore, the increase in testing temperature to 1050 °C was accompanied by an 11% increase in strength for material B, in contrast to a 6% reduction in strength for material A, as compared to room temperature.

As can be seen from Fig. 3a and 3b (detailed loading steps are listed in Table S2), compared to material B, material A exhibited more consistent behaviour with increase in testing temperature from RT to 1050 °C. The loading curves of material A (Fig. 3a) exhibit similar shapes under both testing conditions with multiple small load drops observed after fracture. Conversely, at 1050 °C, material B (Fig. 3b) displayed more abrupt, rather than graceful, load drops compared with the RT tests. However, the loading curves of both materials were more similar at room temperature.

In addition to the load drops which occurred during loading, load relaxation during the XCT scans was also observed during the constant displacement (holding) periods applied to the specimens during the scanning process (marked by arrows in Fig. 3a and 3b). These load relaxations showed a dependence on material type, testing temperature and whether the scan was taken before or after peak load. While an in-depth analysis of the load relaxations is considered beyond the scope of the present study, more details can be found in the Supplementary Materials.

3.3. Failure modes at RT and 1050 °C

Having studied the pre-failure microstructure and the load vs. displacement curves, a thorough view of the material behaviour can be gained by a detailed analysis of the failure modes captured with *in situ* XCT. For material A at RT, using sample A-RT-1 as an example, the specimen was able to sustain a load as high as 0.88P_U (scan taken at step 4, 58 N, in Table S2) while a large number of cracks were already observed. Three major types of cracks are highlighted in Fig. 4a-c: Type I, interfacial cracks formed at the interface between fibre tows and matrix and between orthog-

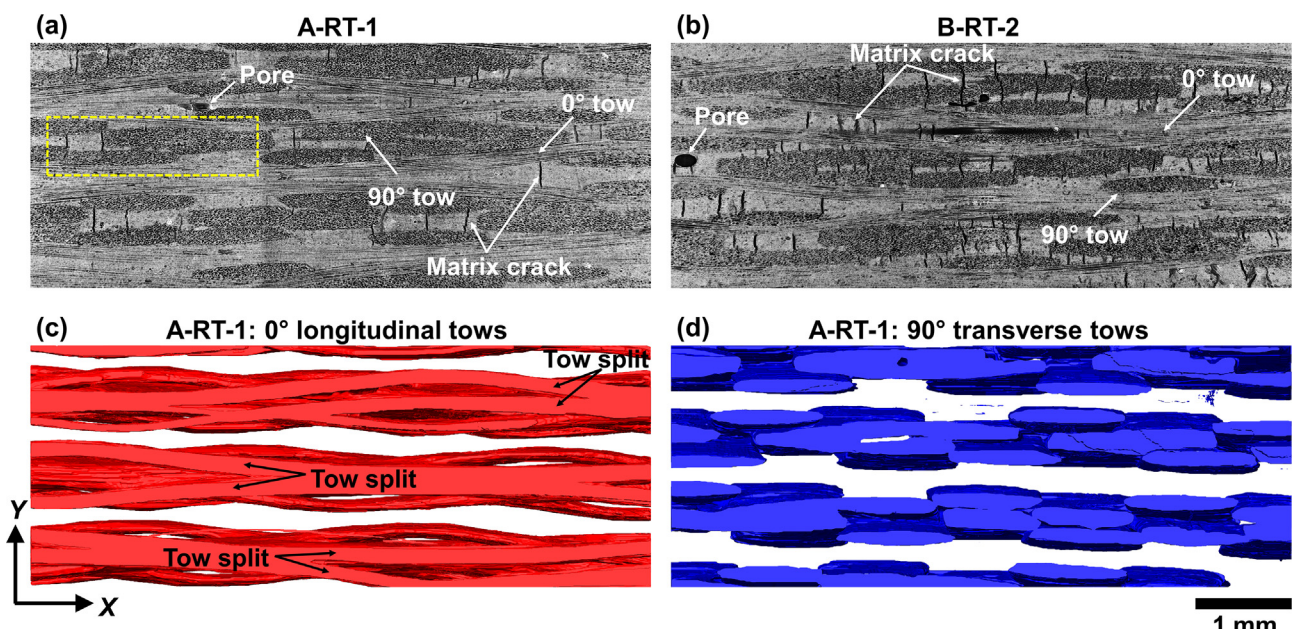


Fig. 2. (a)–(b) Slices of A-RT-1 and B-RT-2 revealing the microstructural features: 0° tows, 90° tows, matrix shrinkage cracks and pores; (c)–(d) segmented fibre tows of A-RT-1 highlighting tow splitting. Note: the dashed yellow rectangle in the case of A-RT-1 indicates the field of view used for the fracture analysis (Fig. 4a–c) and DVC analysis (Fig. 10a–g).

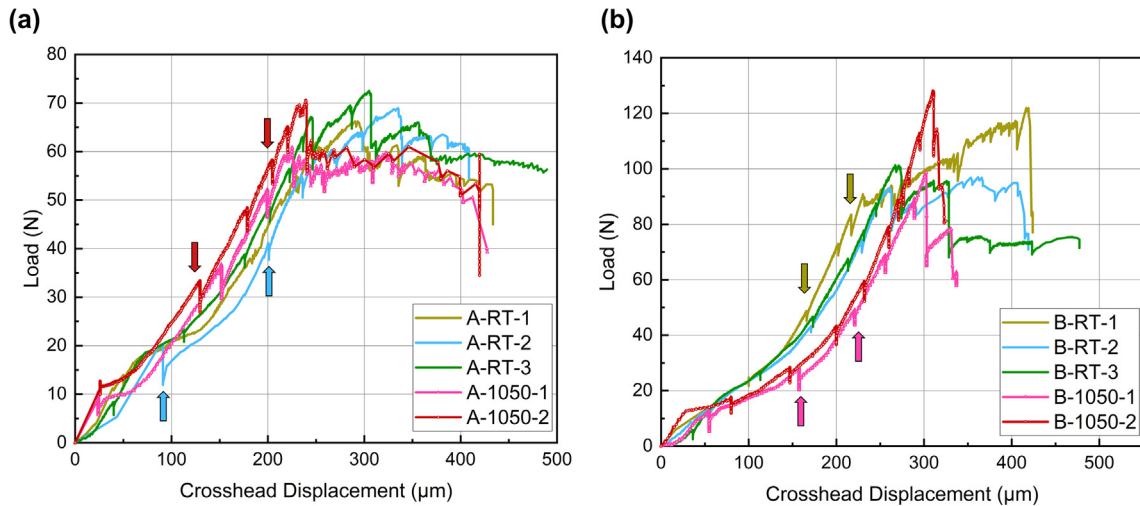


Fig. 3. (a)-(b) Load vs. crosshead displacement for materials A and B, respectively. The coloured arrows indicate locations of XCT scans and the associated load relaxations.

Table 1
Mechanical properties of the two CMC material systems.

| Material | Test Temperature | No. of Specimens | Flexural Strengths (MPa) |
|----------|------------------|------------------|--------------------------|
| A | RT | 3 | 57.2, 59.1; 60.2 |
| A | 1050 °C | 2 | 50.8; 59.7 |
| B | RT | 3 | 104.2; 86.4; 90.3 |
| B | 1050 °C | 2 | 92.8; 114.8 |

onal 0° and 90° fibre tows (orange arrows), *Type II*, inclined cracks exclusively within the 90° fibre tows (yellow circles), and *Type III*, the opening of some, but not all, matrix shrinkage cracks (red arrows). It is important to note that diagonal cracking within the 0° fibre tows was not observed. The presence of these three major

types of cracks formed connected 3D crack patterns where the vertical matrix cracks seem to facilitate the propagation of cracks in the 90° fibre tows and crack deflection at the matrix/fibre interface. At locations where the fibre tows cross, the growing cracks in the 90° bundle tend to deflect along the 0° fibre tows.

At 1050 °C (A-1050-1; Fig. 4d-f; step 6, Table S2, 55 N), *Type I* cracks, either at the 0°/90° or the matrix/90° interfaces, were found to dominate. Note that there are far fewer cracks formed inside the 90° tows compared with corresponding behaviour at room temperature. The *Type II* cracks circled in Fig. 4d and 4f are inclined at a much lower angle than the 45° angle observed at RT and they tend to be closer to the interfaces. Different from the RT specimens, crack initiation at 1050 °C appeared to be in areas where few vertical cracks were present, i.e., matrix cracks are not essential in the formation of cracks at 1050 °C.

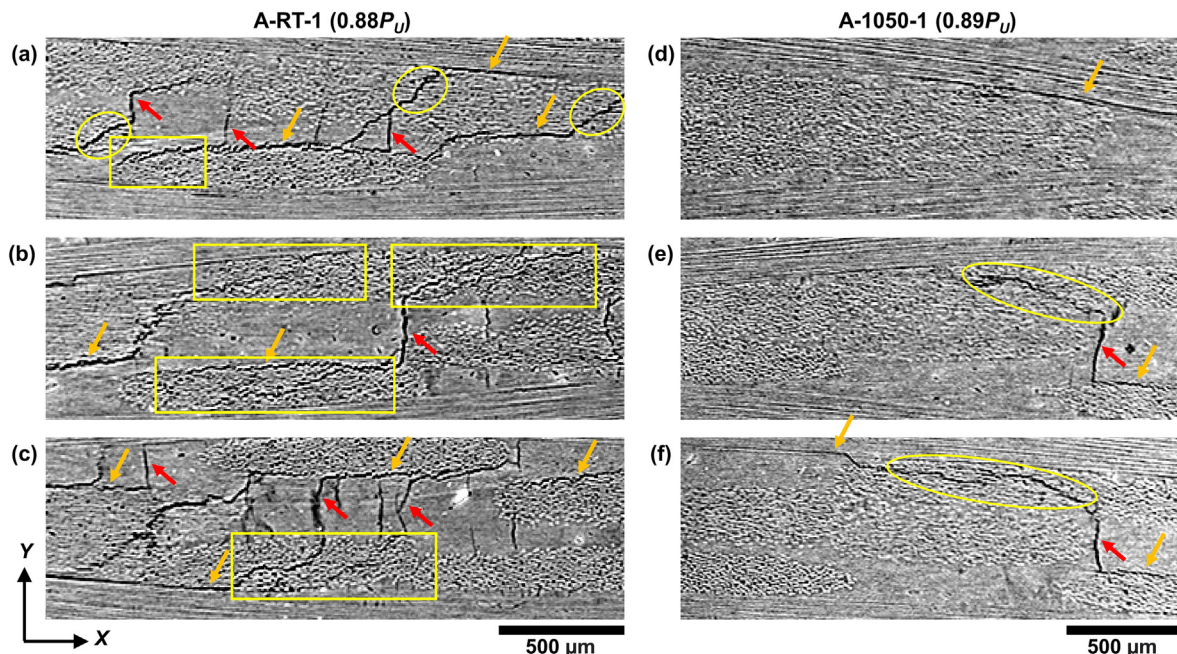


Fig. 4. (a)-(c) Fracture patterns in material A at RT (A-RT-1) and (d)-(f) at 1050 °C (A-1050-1). Orange arrows indicate *Type I* interfacial cracks; yellow circles marking *Type II* inclined intra-tow cracks; red arrow *Type III* matrix cracks and yellow rectangle microcracks (parallel cracks or bifurcation). Note: the area investigated for specimen A-RT-1 was in the middle of the specimen on the left-hand side of the DVC field of view presented in Fig. 1. This area was also highlighted in Fig. 2a using a open dashed rectangle. For A-1050-1, the area was located in the middle of the specimen on the right-hand side of the DVC field of view presented in Fig. 1.

At both RT and 1050 °C, however, extrinsic toughening mechanisms such as crack deflection and uncracked-ligament bridging were observed. It is difficult to give an exact quantification, but the RT damage tends to involve more parallel cracks and crack bifurcation, especially for those formed within the 90°fibres (rectangular areas in Fig. 4). In general, the number of cracks formed at RT seems to be higher than at 1050 °C with more microcracks distributed in the damaged volume. However, at 1050 °C there are fewer but more dominant cracks.

Fig. 5 illustrates an additional type of cracking only observed for material A at RT, namely vertical matrix cracking in areas without pre-existent shrinkage cracks. The left-hand column shows the areas during the pre-load scan whilst the right-hand column shows the same areas upon fracture with the slices equally spaced at

350 µm. Using the same notation for Type III cracks (red arrows), Fig. 5a and 5d as well as Fig. 5c and 5f indicate the presence of shrinkage cracks with subsequent Type III cracking, while Fig. 5b and 5e (located at equal distance from the previous pairs) show a distinct vertical matrix crack in an area without previous shrinkage cracking.

At RT, cracking in material B was considerably less pronounced than in the case of material A (Fig. 6a-c; step 8, Table S3, 90 N). Type I cracking was limited and can only be seen in Fig. 6a. Uncracked-ligament bridging and crack bifurcation inside the 90°tows is visible in Fig. 6b and 6c. Furthermore, the fracture appears to have occurred in an area with a moderate amount of vertical matrix cracks. The opening of such cracks appears partly suppressed in material B, as illustrated in Fig. 6b. Finally, the specimen

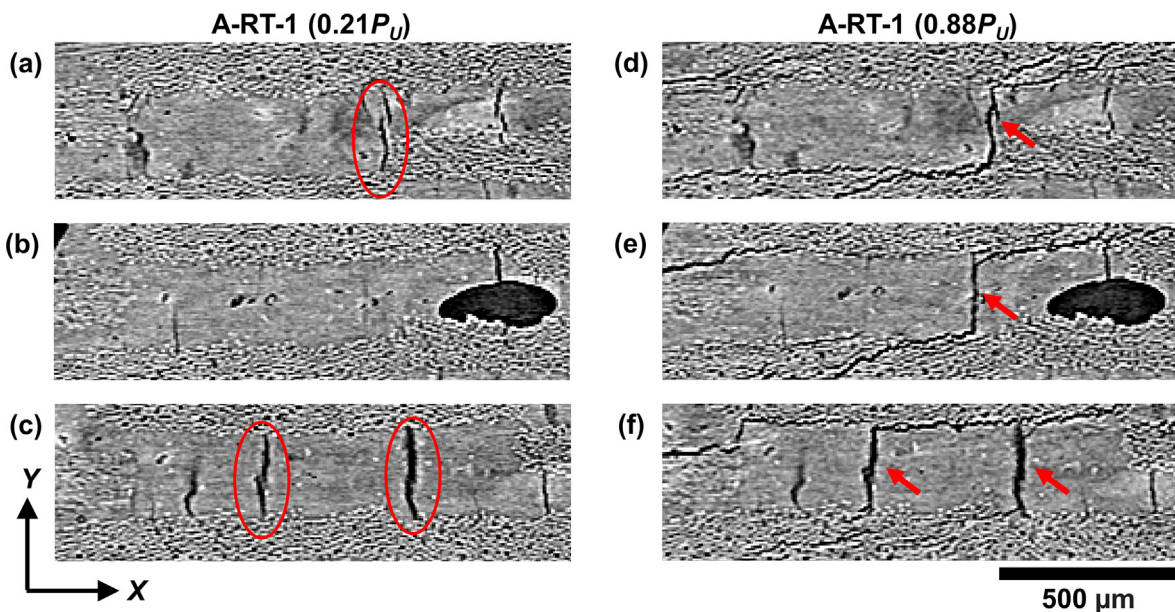


Fig. 5. Vertical matrix cracking in an area without of shrinkage cracks imposed by adjacent Type III cracks. Red circles indicate pre-existent matrix shrinkage cracks and red arrows indicate Type III cracking.

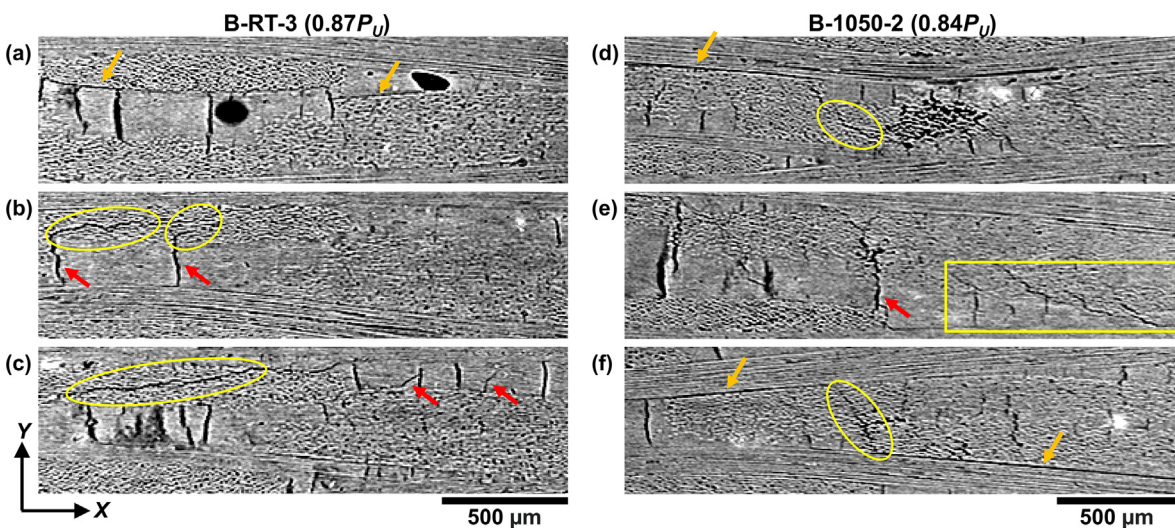


Fig. 6. (a)-(c) Fracture patterns in material B at RT (specimen B-RT-3) and (d)-(f) at 1050 °C (B-1050-2). Orange arrows indicate Type I interfacial cracks; yellow circles Type II inclined intra-tow cracks; red arrows Type III matrix cracks, and yellow rectangle microcracks (parallel cracks or bifurcation). Note: the area investigated for B-RT-3 was located near the compression side of the specimen on the left-hand side of the DVC field of view presented in Fig. 1. For B-1050-2, the area was in the middle of the specimen on the right-hand side of the DVC field of view presented in Fig. 1.

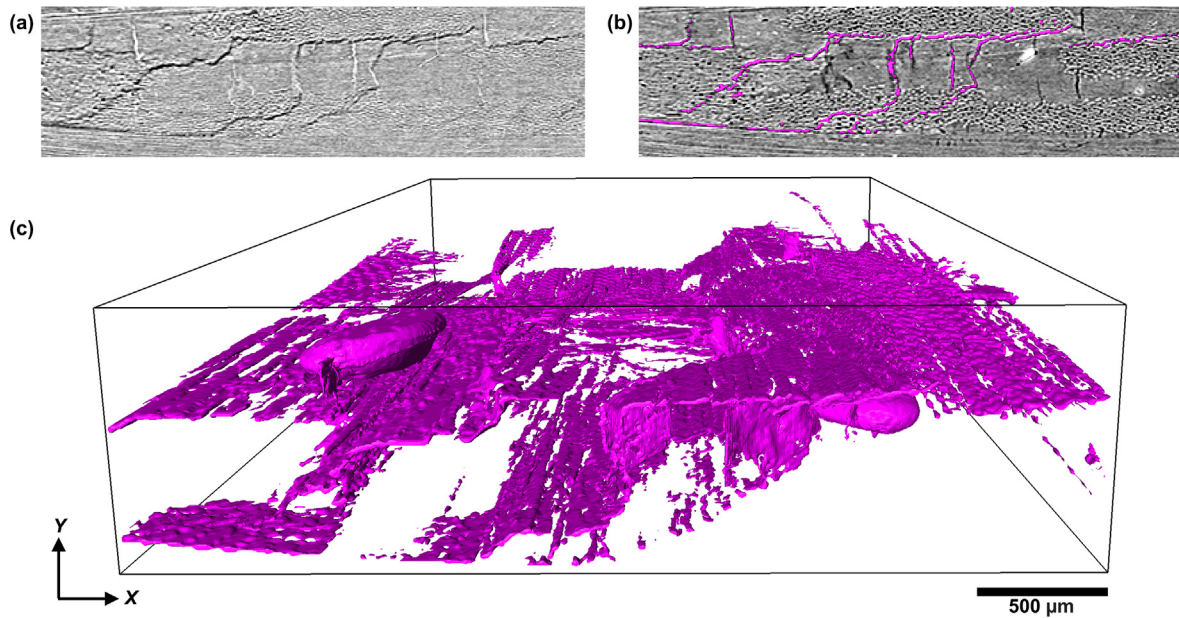


Fig. 7. (a) Slice of the image of the A-RT-1 sample as seen in Fig. 4c with the macrocracks highlighted in purple using the residual field; (b) residual image of the same slice; (c) 3D representation of the analysed crack segmented from the residual field of global DVC on A-RT-1 (step 1 – step 4 in Table S2); shown through the entire width of the specimen.

exhibited very distinct Type III diagonal matrix cracking (red upward pointing arrows in Fig. 6c) extending in an area between 0° and 90° fibres around the pre-existing matrix shrinkage.

At 1050 °C, Type I cracking in material B was primarily observed at the interface between 0° and 90° tows (Fig. 6d and 6f, step 11, Table S3, 108 N). Type II cracking was once again observed within the 90° fibres. The most obvious Type II crack, circled in Fig. 6d, displays multiple changes in the propagation angle appearing almost vertical in Fig. 6e and is bridged to a second 90° tow through a Type III crack (red arrows Fig. 6e). In Fig. 6f, the same intra-tow crack can be seen to directly connect two Type I cracks. In contrast to RT behaviour, at 1050 °C a very distinct area of parallel cracking at 45° angles inside the 90° tows can be seen (rectangle in Fig. 6e). These cracks displayed connections to diagonal matrix microcracks similar to those present in Fig. 6c.

Note that, in addition to visual inspection of the crack patterns, the residual field generated by global DVC was used to identify cracks more accurately; for instance, Fig. 7a is a residual image for sample A-RT-1, and it was overlaid onto the XCT slice to highlight the cracks as seen in Fig. 7b. Further, a full segmentation of the cracks in 3D space (Fig. 7c) showed that cracks formed on the x-y plane extended through the z-direction across the out-of-plane thickness and connected with macropores (Fig. S4).

3.4. Digital volume correlation

3.4.1. Sensitivity studies of the strain uncertainty

Before applying DVC to loaded datasets from the bend tests on the oxide-oxide CMCs, a sensitivity study was necessary to determine the uncertainty and error associated with the method within the context of such materials. The first part of the sensitivity study utilised repeat scans taken under the same loading conditions, as discussed in the Experimental section. For the local DVC analysis, the number of multi-pass steps was increased from 0 to 4 steps. The mean strains, ε_{xx} , ε_{yy} , ε_{zz} were calculated and are compared to the global approach (initiated with the analogous 4-step multi-pass) in Fig. 8. The ε_{xx} strain shows little change with increasing number of multi-pass steps in the local DVC and a slight

reduction using global DVC. The ε_{yy} strain can be seen to decrease from 0- to 2-step multi-pass before slightly increasing in the 4-step MP multi-pass and the global approach. In the case of ε_{zz} , however, the 2- and 4-step multi-pass local and global DVC analyses yielded similar values which were significantly higher than 0-step and 1-step multi-pass local DVC. While the exact cause for the sharp increase in high through-thickness ε_{zz} remains unclear, the maximum strain values calculated using the 1-step multi-pass procedures are approximately 50 microstrain ($\mu\epsilon$), i.e., more than an order of magnitude smaller than the failure strains in the tested specimens. This indicates that for the current oxide CMCs, the 1-step multi-pass local DVC analyses are advantageous. The local DVC correlation coefficient, C_{LA-DVC} , yielded values of $\sim 0.8 \pm 0.1$, independent of the number of steps; the average global correlation

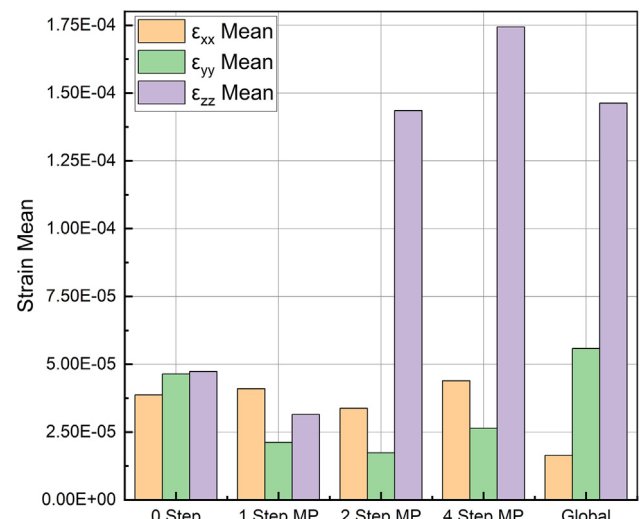


Fig. 8. The change in calculated mean strains for repeat scans using different steps (0 to 4) in multi-pass (MP) method embedded in the local DVC analysis, as compared with those derived with the global DVC analysis.

residual represented 5.9% of the dynamic range of the reference dataset, indicating a satisfactory quality of correlation.

In addition to the analysis of repeat scans, virtual deformation was applied to one of the datasets. Results for the dataset with 0.01 virtual strain applied in three directions (*i.e.*, $\varepsilon_{xx} = \varepsilon_{yy} = \varepsilon_{zz} = 0.01$) are shown in Fig. 9. The addition of multi-pass steps was found to greatly improve correlation. For instance, the average C_{LA-DVC} was more than doubled from 0.43 to 0.97 when using the 1-step multi-pass local DVC compared with the 0-step multi-pass local DVC (Fig. 9a); the strain uncertainties were also reduced by factors of approximately 17 (ε_{xx}), 3 (ε_{yy}) and 7 (ε_{zz}) (Fig. 9c). Increasing the number of multi-pass steps brought no improvement in the correlation coefficient and uncertainty in ε_{yy} but did improve the uncertainty in ε_{xx} and ε_{zz} by a further factor of 2.

The improvement in the strain uncertainty with a multi-pass approach was observed for all virtually deformed cases, with the effect becoming more pronounced at higher prescribed strains. More importantly, however, it was found that initialisation of the global DVC method with either the 1-step or 4-step multi-passes yielded virtually identical results, supporting the findings of the first sensitivity analysis, *i.e.*, the 1-step multi-pass approach is advantageous for the initialisation of global DVC. Further, a decrease in the strain uncertainty at higher prescribed strains for the global DVC can be seen in Fig. 9d. The average percent errors

over the entire range of imposed strains were 0.8% (ε_{xx}), 2.5% (ε_{yy}) and 0.8% (ε_{zz}) for the global DVC. These values were similar to the 1-step multi-pass local DVC and represented a five-fold improvement over the 0 step multi-pass local DVC analysis. Average correlation residuals from global DVC, R_{GA-DVC} , were approximately 3% of the dynamic range of the reference datasets for all the virtually deformed cases; the majority of the values were concentrated around 0, indicating good correlation (Fig. 9b).

3.4.2. DVC analysis of the *in situ* XCT datasets of oxide CMCs

After establishing the uncertainties and errors associated with DVC, the strain fields ensuing from the correlation of loaded datasets can be investigated more accurately. However, as opposed to the virtual deformation calculations, multi-pass local DVC analysis on the *in situ* scans did not significantly improve correlation or the quality of results. For comparative purposes, in the case of material A, sample 1 tested at RT (A-RT-1), the non- multi-pass and 4 step multi-pass approaches for loading Step 1 (14 N) to loading Step 2 (54 N) correlation (Table S2) both yielded correlation coefficients of 0.73. Thus, based on the results of the sensitivity analyses, the global computations of *in situ* datasets were initialised using a modified 1-step multi-pass local DVC approach, as described in Section 2.2.2.

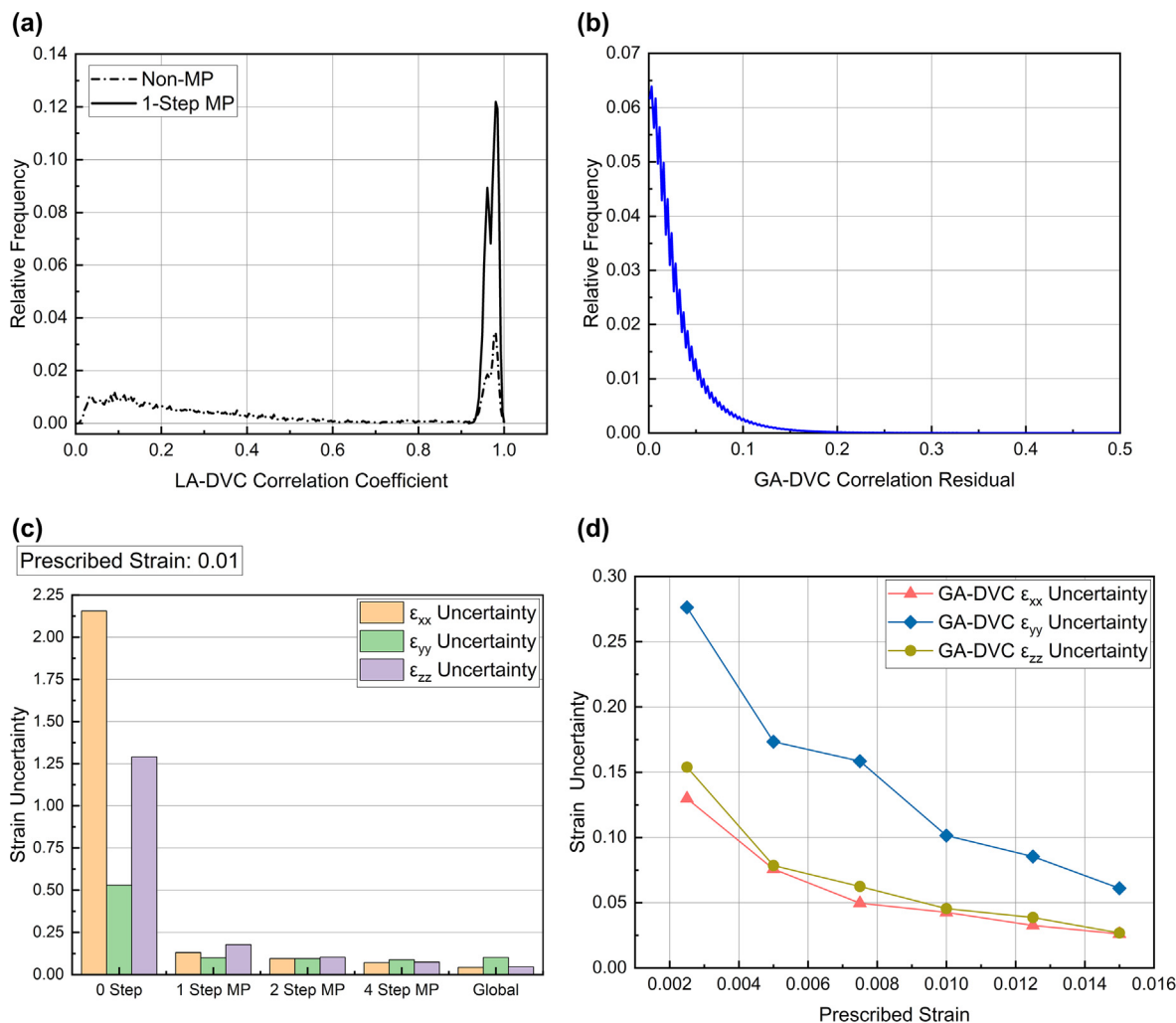


Fig. 9. (a) Comparison between non-multi-pass (MP) and 1-step multi-pass C_{LA-DVC} for the 0.01 virtual strain; (b) R_{GA-DVC} for 0.01 virtual strain; (c) the influence of the multi-pass approach on the strain uncertainty for the 0.01 virtual strain (note: global DVC results initiated with 1-step and 4-step multi-pass local DVC were virtually identical and are thus presented as a single dataset); (d) strain uncertainty as a function of prescribed strain for the global DVC.

In general, the correlation of scans of the same sample at increasing loads and with changing microstructural features due to fracture processes naturally resulted in smaller C_{LA-DVC} values than the virtual deformation calculations. The highest values, usually around 0.75, were recorded for computations of small loading steps with no damage. Conversely, the lowest values occurred in cases of high loading steps with damage present and ranged from

0.55 to 0.65 depending on the extent of damage. Within a single specimen, C_{LA-DVC} was highest in areas where the microstructure of the sample provided sufficient contrast for correlation, i.e., areas with more features. Furthermore, reconstruction artefacts (e.g., ring artefacts) also contributed to the lowering of the correlation mean, as they were specific to each scan. Such artefacts also gave rise to pronounced minima and maxima, i.e., areas of poor correla-

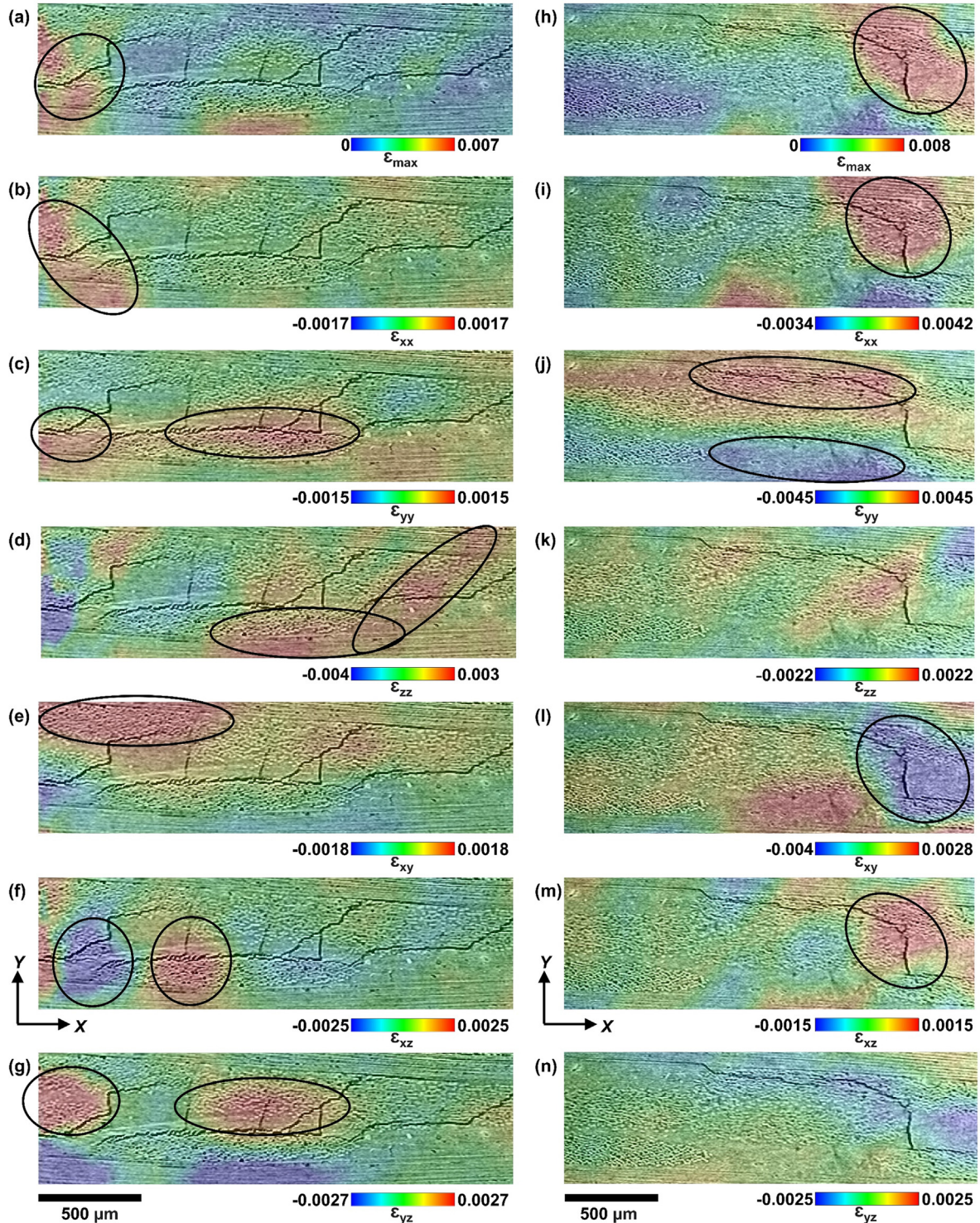


Fig. 10. (a)-(g) Step1 (14 N) – Step2 (54 N) global DVC strains within material A tested at RT (A-RT-1) superimposed on the slice shown in Fig. 4a; (h)-(n) Step1 (9 N) – Step3 (52 N) global DVC strains within material A tested at 1050 °C (A-1050-1) superimposed on the slice shown in Fig. 4f. The strains were calculated prior to crack formation but are plotted on XCT slices showing fracture cracks to highlight correlation between localised strain and crack distribution.

tion in the residual images of the global computations. Similar observations were made for the global DVC analyses whereby small loading steps without any damage present yielded R_{GA-DVC} values of ~5.5% while the value jumped to ~8.5% for higher loading steps with crack formation.

Moreover, characterisation of the failure modes in the two material systems may be further enhanced by analyses of the local DVC strain fields in the respective fracture areas. The computed strain distributions are shown for representative areas of material A tested at room temperature (Fig. 10a-g) and at 1050 °C (Fig. 10h-n) and for the corresponding B material at the same temperatures

(respectively, Fig. 11a-g and h-n). Note the strains were calculated at similar load levels from scans prior to failure and crack formation. The contours are plotted on a dataset where cracks had formed to explore the correlation between localised strains and crack distribution.

The ε_{zz} strain was primarily identified as the highest local normal strain component at room temperature in both composites (e.g., A-RT-1 (0.003 or 0.3%) and B-RT-3 (0.003 or 0.3%)); indeed, the ε_{zz} strain in the A (Fig. 10d) and B (Fig. 11d) materials showed an inclined angle and discontinuity at the fibre/matrix interface. Further, in material A, high ε_{zz} strains were found at the 0/90° fibre

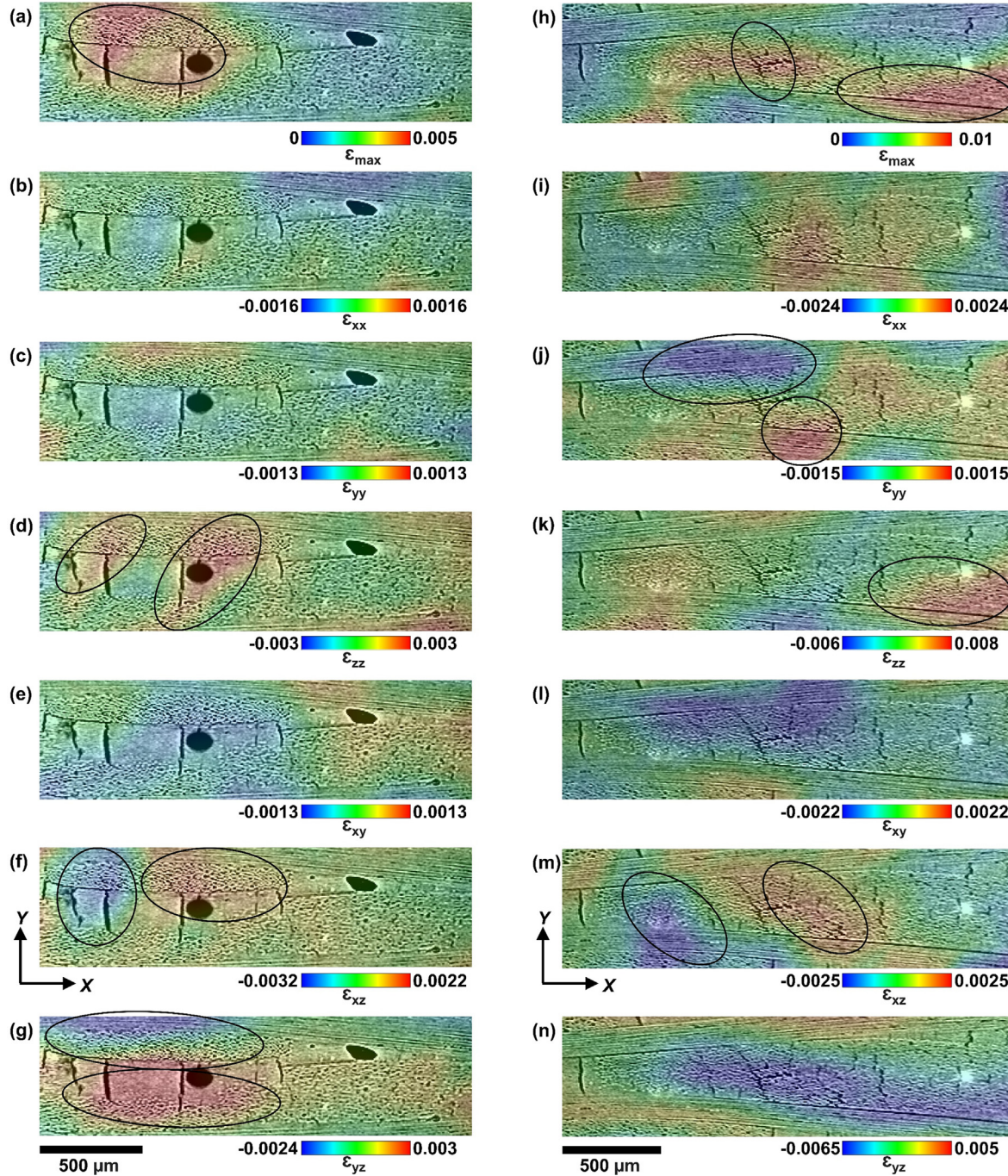


Fig. 11. (a)-(g) Step1 (6 N) – Step6 (87 N) global DVC strains within material B tested at RT (B-RT-3) superimposed on the slice shown in Fig. 6a; (h)-(n) Step1 (17 N) – Step9 (113 N) global DVC strains within material B tested at 1050 °C (B-1050-2) superimposed on the slice shown in Fig. 6f. The strains were calculated prior to crack formation but are plotted on XCT slices showing fracture cracks to highlight correlation between localised strain and crack distribution.

tow interface, but no large crack formation was detected at RT. The ε_{zz} strains in material B also appeared to have a higher concentration at either the 90°/matrix interface at room temperature (B-RT-3, Fig. 11d) or at the 0/90° fibre tow interface at 1050 °C where Type I interfacial cracks were formed (B-1050-2, Fig. 11k). In these cases, the crack fronts highlighted by areas of high ε_{zz} were found to have propagated through the entire width of the specimens (similar to Fig. 7 and Fig. S3).

At 1050 °C, the highest local normal strains in material A (e.g., A-1050-1) were ε_{xx} (0.0042 – Fig. 10i) and ε_{yy} (0.0045 – Fig. 10j). The former (ε_{xx}) correlated well with the maximum principal strain (ε_{max}) distribution (Fig. 10h) and was present at the deflection point of a Type II inclined intra-tow crack through a Type III opening matrix crack. The latter (ε_{yy}) displayed very distinct horizontal banding (i.e., areas of pronounced positive values with abrupt transitions to negative values); tensile values (0.0045) were present along the entire length of the aforementioned Type II inclined intra-tow cracks with the compressive values (-0.0045) present within the matrix between 0° and 90° tows. In this case, the investigated crack front only propagated through approximately half the width of the specimen.

A second notable observation was the consistent banding of shear strains in both materials systems. This is most clearly visible at RT for the ε_{xz} (Fig. 10f and 11f) and ε_{yz} (Fig. 10g and 11g) strains. For the ε_{xz} strain, hard transitions from positive values in the middle of 90° tows to negative values to the edges of the same tows can be observed in materials A (Fig. 10f) and B (Fig. 11f), while for the ε_{yz} strain, positive values distributed horizontally in the matrix between different 90° tows changed abruptly to negative values at the 0/90° interface and propagated further into the 0° fibres (Fig. 10g for material A at RT and Fig. 11g for material B). Both ε_{xz} and ε_{yz} banding in both materials A and B at RT was present in areas of Type I interfacial cracks, either at the fibre/matrix or at the 0/90° fibre bundle interface. At 1050 °C, diagonal banding of the ε_{xz} shear strain was observed predominantly in material B (Fig. 11m) and to a lesser extent in material A (Fig. 10m). Similar to the distribution of shear stresses in RT tests, positive shearing in material B at 1050 °C (0.0025) was present inside the 90° tows while negative shearing (-0.0025) was present at the edge of the 90° tows. As opposed to RT tests, banding at 1050 °C was associated more with vertical cracks: Type II and Type III for material A (Fig. 10m) and Type II for material B (Fig. 11m). Material A also displayed very pronounced banding of the ε_{xy} strain. Both the positive and negative values were present in regions of the matrix with the negative shear strains correlating well with the formation of Type III cracks.

4. Discussion

4.1. Application of DVC to oxide CMCs

The two sensitivity studies revealed important insights into the advantages and limitations of the application of DVC analysis to oxide CMCs. The natural features of the fibres, matrix and pores in these materials provided a very suitable medium for DVC analysis. However, the repeat scan analyses showed an inherent limit on the correlation quality, with C_{LA-DVC} never surpassing 0.8. If normalised to this range (0–0.8), the C_{LA-DVC} values on loaded specimens change from 0.55–0.75 to 0.69–0.94, thus indicating a smaller impact of loading on the quality of DVC than it was initially estimated. The residuals from global DVC analysis, R_{GA-DVC} , showed a similar behaviour; the 6% value for repeat scans was almost equal to the lowest residual computed for loaded scans. As such, there are several primary factors that negatively affect correlation when applying DVC to oxide-oxide CMCs.

The first is represented by areas of low contrast within a specimen (mainly in the case of longitudinal 0° tows) due to the testing alignment, i.e., the attenuation of X-rays along the length of a specimen will be greater than its width direction and the use of white light as opposed to monochromatic light (a choice made in order to reduce exposure time and allow more scans to be taken). A second factor is reconstruction artefacts, e.g., ring artefacts; elimination of these artefacts through the use of different algorithms comes at the expense of detail. Lastly, akin to all image based correlation methods, fracture phenomena represent a violation of continuity due to the formation of cracks and, as such, can cause erroneous correlations, although this is usually only the case for large cracks.

It should be emphasized that the correlation C_{LA-DVC} values were very satisfactory for the virtual deformation test ($\varepsilon_{xx} = \varepsilon_{yy} = \varepsilon_{zz}$); in this respect, the use of a stepped multi-pass approach for the local sensitivity analysis proved successful in improving the correlation qualities and reducing the strain uncertainties and percent error. Higher prescribed strains with higher displacements saw the most drastic improvements, although for the current oxide CMCs, the strains were mostly less than 0.01. However, these results did not translate to the datasets subjected to flexural deformation. Multi-pass approaches did not seem to have any significant effects on the correlation quality and strain calculations. A potential explanation for this are the very low mean strains recorded in pre-failure scans. For example, Step 1 (14 N) to Step 2 (54 N) (Table S2) using local DVC analysis for material A at RT yielded mean values of 4.1 $\mu\varepsilon$ (ε_{xx}) and 180 $\mu\varepsilon$ (ε_{yy} and ε_{zz}) which are considerably lower than the lowest prescribed strain of 2500 $\mu\varepsilon$. Based on the less pronounced effect of a multi-pass procedure on low prescribed strains as evidenced by the sensitivity analysis, it appears unlikely that such a method would have a major overall effect on the computed strains of loaded datasets. Nonetheless, isolated strain concentrations during *in situ* bending may in some cases exceed 2500 $\mu\varepsilon$ and therefore the multi-pass approach outlined through the sensitivity studies is recommended for the initialisation of global DVC in order to reduce strain uncertainty and error. Results from the global DVC analysis were in agreement with the corresponding local DVC results, and added the advantage of continuity to improve visualisation. Additionally, as is evident from the higher strain uncertainty (Fig. 9) and percent error along the z dimension, a certain level of anisotropy in the DVC sensitivity was present. This suggests that for users applying DVC to oxide CMCs, the sensitivity study on virtually strained datasets has to be used with caution; specifically, for the optimisation of results, an analysis on deformed datasets has to be carried out. This requirement is potentially applicable to all CMCs, including SiC-based systems.

However, DVC was extremely successful in locating and quantifying strain concentrations before failure (Figs. 10 and 11). As such, the locations of maximum principal strains (ε_{max}) formed is a reliable indicator of crack initiation. Strain values after failure though need to be analysed very carefully and very critically; the fact that the continuity is violated in the cracked regions can result in poor correlation and thus potentially erroneous strain values. Notwithstanding, the violation of continuity provides a significant advantage by indicating the incipient evidence of cracks in the residual fields of the DVC analysis. Features which may otherwise go unnoticed can thus be segmented from rest of the specimen. This property was extensively used in the current study when analysing the fracture patterns (Fig. 7).

It should be noted that the 3.25 μm voxel size resolution used in the current study, coupled with a down-sampling by a factor of 1.8 resulted in a voxel size of 5.85 μm , i.e., approximately 2 voxels per fibre (the fibre diameter was ~10–12 μm). This does not generate a sufficient level of detail for DVC analyses at fibre length-scales and therefore the sub-volume size for local DVC and the mesh size for

global DVC were optimised to capture the behaviour at the length-scale of the fibre tows. For DVC at the fibre level, considerably smaller DVC interrogation windows and a higher XCT magnification would both be required.

4.2. Mechanical properties and failure modes at RT and 1050 °C

Flexural strength data for similar materials are not readily available in the literature. The strength results for the present composites, presented in Table 1 and Fig. 3, however, are considerably lower than the one set of tensile data that is available, which reports values of ~170 MPa at RT and 190 MPa at 1200 °C [15]. A major contributing factor to this observation may be the pronounced effect of shear stresses which were caused by the low ratio between loading span and in plane width of the specimens (7:1).

Despite similarities in the cracking mechanisms and strain distributions, a significant consequence of the different sintering temperatures of the present two systems was found within the considerably higher failure loads of material B, which was sintered at a slightly higher temperature. At comparable load levels after failure, the material B generally exhibited one major area of fracture, as opposed to material A which exhibited more distributed damage with multiple and more pronounced regions and with the vertical propagation of cracks facilitated by shrinkage cracks. Furthermore, the behaviour of material A was similar at room temperature and at 1050 °C, with smaller variations in both the failure loads and the pre-failure maximum principal strains, e.g., $\varepsilon_{\max} = 0.007$ for A-RT-1 (Fig. 10a) and 0.008 for A-1050-1 (Fig. 10h) both located in the matrix surrounding the 90° fibres. Failure in material B occurred at higher loads at 1050 °C and was also more brittle under these conditions. Values of the ε_{\max} strain were considerably higher in material B at 1050 °C (0.01 in Fig. 11a) than at RT (0.005 in Fig. 11h), but both principal strains were concentrated within the 90° fibres, thus highlighting another difference between the two composite materials. Finally, the load relaxations after peak load indicated different stress relaxation mechanisms for the two materials despite their similar processing parameters. The exact mechanisms, however, remain unclear and future experiments targeting this area will be needed for a thorough understanding.

A potential source of variability in the properties of the two composite systems may arise due to the tension side of some specimens being dominated by 0° fibres while for others it may be 90° fibres. Therefore, when analysing the different failure patterns across the testing iterations, it is imperative to consider not only environmental effects but also specific local microstructural features. Thus, below we discuss the link between the observed microstructure, DVC observations and failure modes.

In all cases, the highest degree of damage was observed as Type I interfacial cracking within the middle of the specimen and directly above the support rollers. In order to understand these observations, the pre-failure maximum principal strains resulting from the global DVC analysis were investigated in these areas of interest. ε_{\max} maxima were invariably present in such areas of damage but only on the edges of the specimens and were consequently considered as good fracture criteria for crack initiation in the current materials. Analysis of the strain components in areas of ε_{\max} maxima was also very telling.

The propensity for strain accumulation along the z-axis in the context of a y-axis three-point bending test could be rationalised by minor imperfections in the testing geometries. Such imperfections can lead regions of increased loading and thus create local strain concentrations. Thus, the ε_{zz} strain appears to be the driving force behind the out-of-plane lateral propagation of cracks in both materials. While a clear distribution pattern cannot be established,

it does appear that tensile ε_{zz} is concentrated around the edges of 90° tows, exploiting a potentially weaker bonding area of matrix/90° or 0/90° fibres to cause sliding and elongation. The bonding strength between the constituents may be an important factor behind for the banding of shear strains. As load is applied, the strain accumulated around the 90° fibres is dictated by the surrounding environment. In cases where both matrix and 0° fibres are directly bonded to the 90° fibres an abrupt strain gradient is formed while instances in which only 0° fibres surround the 90° ones appear to lead to higher shear strain values. This can be seen by comparing the ε_{yz} strains in material B at RT (B-RT-3 in Fig. 11g) vs. 1050 °C (B-1050-2 in Fig. 11n).

The highest shear component in material A at 1050 °C, namely ε_{xy} , was clearly located in areas of the matrix but with different surrounding microstructural environments (Fig. 10l). The banding in this case may be rationalised by inspecting the normal strains ε_{xx} and ε_{yy} (Fig. 10i and 10j). The former shows a very pronounced tensile region of across both 0° and 90° fibres as well as matrix but is most importantly present at the top of a Type III crack. The latter is distinctly located along the 0/90° interface where fracture was observed. The matrix, as the most compliant component, accommodated the shear strain resulting from the concurrent action of the two direct strains.

It should be noted that although not all test specimens of either composite showed deflection through shrinkage cracks in the crack initiation areas, all of them did exhibit such behaviour at different locations as can be seen in Figs. 4 and 6. This is relevant because it highlights shrinkage cracks as an important energy dissipation pathway for cracks, preventing fibre fracture. However, the extent to which shrinkage cracks influence crack formation appears to be less substantial, as can be seen in the failure locations for material A at high temperatures (e.g., specimen A-1050-1, Fig. 4d-f) where the concentration of shrinkage cracks was considerably higher in a part of the specimen that did not fracture on loading. Shrinkage cracks may nonetheless play a role in the formation of new cracks by imposing high stress concentrations on the matrix as was evidenced in the case of material A at RT by Fig. 5. It appears that in areas of pronounced but interrupted shrinkage cracks which have undergone Type III cracking, the stress concentrations imposed by the sharp shrinkage cracks lead to vertical cracking of the matrix as a pathway to connect the adjacent equidistant Type III cracks. The distribution of shrinkage cracks inside material A and material B at RT was more uniform but still differed considerably from specimen to specimen. Despite the two materials having different sintering temperatures, noticeable differences in shrinkage cracking between them were not identified. The variable degree of shrinkage cracking across the composite plates may thus be a consequence of uneven sintering kinetics caused by the local microstructures allowing different degrees of matrix expansion. A further consequence of this may be the development of highly variable residual stress distributions. Residual stresses have previously been shown to have significant effects, not only on the bulk properties of the material but also on the cracking behaviour [45].

4.3. Micro-mechanisms of fracture at RT and 1050 °C

Microcracking and uncracked-ligament bridging were observed as secondary extrinsic energy dissipation mechanisms. This behaviour was identified primarily within the 90° tows with examples visible in Fig. 4b and 4f and more scarcely within areas of matrix (Fig. 6c and 6e). The nature of microcracking was investigated in all cracking areas along the entire width of the specimens starting from the area of maximum principal strain to reveal three main mechanisms, specifically at the intra-tow, along interfaces and within the matrix.

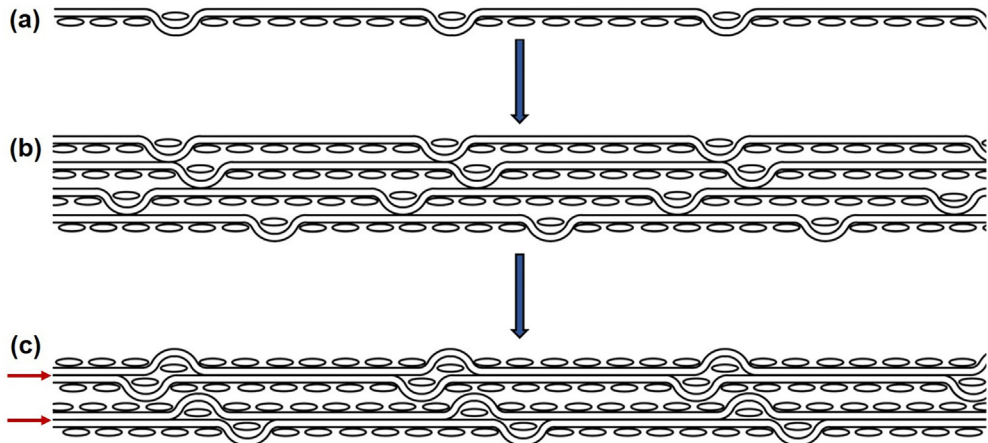


Fig. 12. (a) Side-on view of a single sheet of woven eight-harness satin weave; (b) stacking of multiple sheets without rotation - every longitudinal tow shows contact with both the ones above and under it; (c) stacking of multiple tows with alternating orientation - layering is highlighted with red horizontal arrows.

The primary mechanism was intra-tow microcracking, occurring within a single tow either coalescing into a single crack (bottom rectangle in Fig. 4b) or splitting away from the main crack (top rectangle in Fig. 4b).

A secondary mechanism of microcracking was that of interface microcracking and ligament bridging observed in instances where the edges of two 90° tows came in contact forming multiple parallel microcracks interlinked via ligament bridging. In the example illustrated in Fig. 4b (top right rectangle), a crack within one tow propagated through a small shrinkage crack and deflected at the interface of another tow before edge contact (while this appears as a single area of 90° fibres in Fig. 4b, the right-hand side of Fig. 4c shows two separate 90° tows). On contact, extensive microcracking was observed, essentially causing a transition in crack path to follow the matrix/90° interface.

Fig. 6e shows the third mechanism, namely matrix microcracking, together with the interface mechanism described above. A delamination crack at a 0/90° interface can be seen to have transitioned through matrix microcracking into two adjacent adjoined 90° tows. Upon separation, the multiple parallel cracks were bridged to form a continuous crack which penetrated both newly separated tows. Matrix microcracking can also be seen in Fig. 6c in the form of multiple diagonal cracks.

Interestingly all three types of microcracking were found to occur either through or around shrinkage cracks. It appears that in some cases, shrinkage cracks create additional entry or exit points for crack propagation into the tows at the matrix/90° interface. Ligament bridging subsequently acts as a transfer mechanism upon the joining of microcracks or splitting of a single crack into microcracks. Conversely, matrix microcracking acts as a pathway in instances where 0/90° interfaces are terminated or initiated enabling fracture transfer to or from the 90° tows.

4.4. Implications on the optimised design of oxide-oxide CMCs

As shown in Results section, a striking feature of both these oxide-oxide CMCs is the layering and apparent 'splitting' of both longitudinal and transverse tows. To best understand the tow behaviour, one must first consider the structure of the eight-harness satin weave. Fig. 12a shows the side-on view of a single sheet of tows woven in the aforementioned manner. Stacking of such sheets without any rotation results in remote contact points between every adjacent 0° tow, i.e., there is no layering (Fig. 12b). Conversely, the alternate stacking of individual sheets

results in extended contact between pairs of 0° tows and consequently 'layering' into areas of 0° and 90° tows, as seen in Fig. 2c and 2d. A 0° layer is thus made up of parallel 0° tows, the top of which curve up while the bottom ones curve down (highlighted by red horizontal arrows in Fig. 12c). This sheds important light on the nature of 'tow splitting', suggesting that it is not individual tows which are splitting but rather the outcome of the alternating stacking orientations (Fig. 12c).

A consequence of this stacking arrangement is the creation of large areas of matrix, which in turn enables greater extension of shrinkage cracks on sintering. In the most extreme cases these can extend the full length between layers or between the top and bottom tow of a splitting layer, as illustrated in Fig. 2a and 2b. Moreover, pockets of air, inaccessible to impregnating matrix-precursor slurry, are also formed, resulting in macropores during sintering. Macropores have been shown to be either directly related to fracture or indirectly via shrinkage cracks (Fig. 7c). Such observations indicate that an alternating stacking arrangement can have detrimental effects on the mechanical properties of oxide-oxide CMCs through the formation of features which increase the ease of crack propagation.

These observations highlight the advantages of *in situ* 3D imaging using XCT over *post-mortem* 2D surface techniques (e.g., SEM) for the characterisation and interpretation of the microstructure, damage and fracture behaviour of oxide-oxide CMCs under load at high temperatures.

5. Conclusions

In the current paper, we have investigated the ambient to elevated temperature mechanical behaviours of two iterations of Nextel 720TM/alumina (oxide-oxide) ceramic-matrix composites from the perspective of the suitability of *in situ* full-field displacement and strain mapping via synchrotron X-ray computed microtomography with digital volume correlation.

The sintering temperature had a marked influence on the mechanical behaviour of the two materials. Material A, with a lower sintering temperature of 1200 °C, displayed a considerably lower average flexural strength and more graceful failure both at RT and 1050 °C than material B, which was sintered at a somewhat higher temperature of ~ 1250 °C. Furthermore, the behaviour of material A was more consistent across the two testing temperatures, as opposed to material B which displayed more brittle failure when tested at 1050 °C.

An inherent layering and layer splitting was observed in both materials rationalised by the stacking orientation of dry fibre sheets. The microstructures arising from these stacking arrangements resulted in complex cracking patterns on failure. Three main crack types were identified: *Type I* – interfacial cracks; *Type II* – inclined cracking within the 90° fibre tows (0° fibre tows did not exhibit this type of cracking); *Type III* – the opening of vertical shrinkage cracks (this type may also be associated with the cracking of undamaged matrix). Secondary extrinsic toughening mechanisms were microcracking and uncracked-ligament bridging.

The DVC sensitivity studies demonstrated the method's applicability to oxide-oxide CMCs. The inherent microstructural contrast within such materials provides a very suitable medium for 3-D correlation. Furthermore, the use of global DVC enables the detailed analysis of fracture phenomena through residual images. Areas of maximum principal strain before failure were found to be good predictors for the eventual fracture location. Similar to the loading data, going from RT to 1050 °C, the behaviour of material A was more consistent ($\varepsilon_{\max} = 0.007$ at RT vs. 0.008 at 1050 °C) than in material B ($\varepsilon_{\max} = 0.005$ at RT vs. 0.01 at 1050 °C). The complex microstructures of oxide-oxide CMCs naturally gave rise to similarly complex local straining. While the out-of-plane, through-thickness ε_{zz} was the highest direct strain component present locally in the fracture locations of most test specimens, high local shear strains were ubiquitous across all specimens. The abrupt positive to negative transitions of the shear strain components was deemed to be associated with the differing bonding strengths between 0° fibres, 90° fibres and matrix.

The use of DVC coupled with real time high-temperature X-ray microtomography clearly provides a comprehensive methodology to document and quantify the multiple mechanisms of damage evolution leading to the fracture of oxide-oxide CMCs, thereby providing essential insights into the mechanical behavior of this class of materials especially at realistic service temperatures. The methodology and knowledge generated is critical for improving the design of oxide-oxide CMCs for aerospace applications.

Declaration of Competing Interest

The authors declare that they have no known competing financial interests or personal relationships that could have appeared to influence the work reported in this paper.

Acknowledgements

We would like to acknowledge the EPSRC Grants EP/L016028/1 and EP/T000368/1. The authors are grateful to Tim Shumate and Barrett Jackson at Composites Horizons, LLC (PCC Structural, Oregon, United States, for providing technical support and Composite Horizons, LLC (PCC Structural, USA) for supplying samples. The authors also acknowledge the use of the X-ray synchrotron micro-tomography beamline (8.3.2) at the Lawrence Berkeley National Laboratory's Advanced Light Source, which is supported by the U.S. Department of Energy, Office of Science, Office of Basic Energy Sciences of the U.S. Department of Energy under contract no. DE-AC02-05CH11231. D.L. and R.O.R. would like to thank Dr. Dula Parkinson for help with the synchrotron tomography experiments.

Data availability

The raw/processed data required to reproduce these findings cannot be shared at this time as the data also forms part of an ongoing study.

Appendix A. Supplementary material

Supplementary data to this article can be found online at <https://doi.org/10.1016/j.matdes.2021.109899>.

References

- [1] F.W. Zok, Developments in oxide fiber composites, *J. Am. Ceram. Soc.* 89 (7) (2006) 3309–3324, <https://doi.org/10.1111/j.1551-2916.2006.01342.x>.
- [2] M. Alabdullah, N.M. Ghoniem, Damage mechanics modelling of the non-linear behavior of SiC/SiC ceramic matrix composite fuel cladding, *J. Nucl. Mater.* 524 (2019) 296–311, <https://doi.org/10.1016/j.jnucmat.2019.07.017>.
- [3] H. Ohnabe, S. Masaki, M. Onozuka, K. Miyahara, T. Sasa, Potential application of ceramic matrix composites to aero-engine components, *Compos. Part A – Appl. Sci.* 30 (1999) 489–496, [https://doi.org/10.1016/S1359-835X\(98\)00139-0](https://doi.org/10.1016/S1359-835X(98)00139-0).
- [4] J. Steibel, Ceramic matrix composites taking flight at GE Aviation, *Am. Ceram. Soc. Bull.* 98 (3) (2019) 30–33.
- [5] N.S. Jacobson, E.J. Opila, K.N. Lee, Oxidation and corrosion of ceramics and ceramic matrix composites, *Curr. Opin. Solid. State Mater. Sci.* 5 (2001) 301–309, [https://doi.org/10.1016/S1359-0286\(01\)00009-2](https://doi.org/10.1016/S1359-0286(01)00009-2).
- [6] W. Gauthier, F. Pailler, J. Lamon, R. Pailler, Oxidation of silicon carbide fibers during static fatigue in air at intermediate temperatures, *J. Am. Ceram. Soc.* 92 (9) (2009) 2067–2073, <https://doi.org/10.1111/j.1551-2916.2009.03180.x>.
- [7] F.W. Zok, C.G. Levi, Mechanical Properties of Porous-Matrix Ceramic Composites, *Adv. Eng. Mater.* 3 (2001) 15–23.
- [8] R.J. Kerans, R.S. Hay, T.A. Parthasarathy, M.K. Cinibulk, Interface design of oxidation-resistant ceramic composites, *J. Am. Ceram. Soc.* 85 (11) (2002) 2599–2632, <https://doi.org/10.1111/j.1151-2916.2002.tb00505.x>.
- [9] K.A. Keller, G. Jefferson, R.J. Kerans, Oxide-oxide composites, in: N.P. Bansal, J. Lamon (Eds.), *Ceramic Matrix Composites Materials, Modeling and Technology*, John Wiley & Sons Inc, New Jersey, 2015, pp. 236–272.
- [10] 3M™ Nextel™ Ceramic Fibers and Textiles Technical Reference Guide, 3M Advanced Materials Division, 2020.
- [11] D.M. Wilson, Statistical tensile strength of Nextel™ 610 and Nextel™ 720 fibres, *J. Mater. Sci.* 32 (1997) 2535–2542, <https://doi.org/10.1023/A:1018538030985>.
- [12] M. Schmücker, P. Mechnick, All-oxide ceramic matrix composites with porous matrices, in: W. Krenkel (Ed.), *Ceramic Matrix Composites Fiber Reinforced ceramics and their Applications*, WILEY-VCH Verlag GmbH & Co. KGaA, Weinheim, 2008, pp. 205–229.
- [13] E.A.V. Carelli, H. Fujita, J.Y. Yang, F.W. Zok, Effects of thermal aging on the mechanical properties of a porous-matrix ceramic composite, *J. Am. Ceram. Soc.* 85(3) (2002) 595–602, <http://dx.doi.10.1111/j.1151-2916.2002.tb00138.x>.
- [14] D.T. Di Salvo, E.E. Sackett, R.E. Johnston, D. Thompson, P. Andrews, M.R. Bache, Mechanical characterisation of a fibre reinforced oxide/oxide ceramic matrix composite, *J. Eur. Ceram. Soc.* 35 (2015) 45113–54520, <https://doi.org/10.1016/j.jeurceramsoc.2015.08.032>.
- [15] M.B. Ruggles-Wrenn, J.C. Braun, Effects of steam environments on creep behavior of Nextel™ 720/alumina ceramic composite at elevated temperature, *Mater. Sci. Eng. A* 397 (2008) 101–110, <https://doi.org/10.1016/j.msea.2008.06.036>.
- [16] M.B. Ruggles-Wrenn, S. Mall, C.A. Eber, L.B. Harlan, Effects of steam environment on high-temperature mechanical behavior of Nextel™ 720/alumina (N720/A) continuous fiber ceramic composite, *Compos. Part A – Appl. Sci.* 37 (2006) 2029–2040, <https://doi.org/10.1016/j.compositesa.2005.12.008>.
- [17] J.M. Mehrman, M.B. Ruggles-Wrenn, S.S. Baek, Influence of hold times on the elevated-temperature fatigue behavior of an oxide-oxide ceramic composite in air and in steam environment, *Compos. Sci. Technol.* 67 (2007) 1425–1438, <https://doi.org/10.1016/j.compscitech.2006.09.005>.
- [18] M.B. Ruggles-Wrenn, G.T. Siegert, S.S. Baek, Creep behavior of Nextel™ 720/alumina ceramic composite with ±45 fiber orientation at 1200 °C, *Compos. Sci. Technol.* 68 (2008) 1588–1595, <https://doi.org/10.1016/j.compscitech.2007.07.012>.
- [19] M.B. Ruggles-Wrenn, A.T. Radzicki, S.S. Baek, K.A. Keller, Effects of loading rate on the monotonic tensile behavior and tensile strength of an oxide-oxide ceramic composite at 1200 °C, *Mater. Sci. Eng. A* 492 (2008) 88–94, <https://doi.org/10.1016/j.msea.2008.03.006>.
- [20] E. Maillett, A. Singhal, A. Hilmas, Y. Gao, Y. Zhou, G. Henson, G. Wilson, Combining in-situ synchrotron X-ray microtomography and acoustic emission to characterize damage evolution in ceramic matrix composites, *J. Eur. Ceram. Soc.* 39 (2019) 3546–3556, <https://doi.org/10.1016/j.jeurceramsoc.2019.05.027>.
- [21] A. Morales-Rodriguez, P. Reynaud, G. Fantozzi, J. Adrien, E. Maire, Porosity analysis of long-fiber-reinforced ceramic matrix composites using X-ray tomography, *Scr. Mater.* 60 (2009) 388–390, <https://doi.org/10.1016/j.scriptamat.2008.11.018>.
- [22] Y. Chen, L. Gelebart, C. Chateau, M. Bornert, A. King, P. Aimédié, C. Sauder, 3D detection and quantitative characterization of cracks in a ceramic matrix composite tube using X-Ray computed tomography, *Exp. Mech.* 60 (2020) 409–424, <https://doi.org/10.1007/s11340-019-00557-5>.
- [23] H. Bale, M. Blacklock, M.R. Begley, D.B. Marshall, B.N. Cox, R.O. Ritchie, Characterizing three-dimensional textile ceramic composites using synchrotron X-ray micro-computed-tomography, *J. Am. Ceram. Soc.* 95 (1) (2012) 392–402, <https://doi.org/10.1111/j.1551-2916.2011.04802.x>.

- [24] A.M. Hilmas, K.M. Sevener, J.W. Halloran, Damage evolution in SiC/SiC unidirectional composites by X-ray tomography, *J. Am. Ceram. Soc.* 103 (2020) 3436–3447, <https://doi.org/10.1111/jace.17017>.
- [25] H.A. Bale, A. Haboub, A.A. MacDowell, J.R. Nasiatka, D.Y. Parkinson, B.N. Cox, D.B. Marshall, R.O. Ritchie, Real-time quantitative imaging of failure events in materials under load at temperatures above 1600 °C, *Nat. Mater.* 12 (2013) 40–46, <https://doi.org/10.1038/nmat3497>.
- [26] B.K. Bay, T.S. Smith, D.P. Fyhrie, M. Saad, Digital volume correlation: Three-dimensional strain mapping using X-ray tomography, *Exp. Mech.* 39 (3) (1999) 217–226, <https://doi.org/10.1007/BF02323555>.
- [27] B.K. Bay, Methods and applications of digital volume correlation, *J. Strain Anal. Eng. Des.* 43 (2008) 745–760, <https://doi.org/10.1243/03093247JSA436>.
- [28] A. Buljac, C. Jailin, A. Mendoza, J. Neggers, T. Taillandier-Thomas, A. Bouterf, B. Smaniotti, F. Hild, S. Roux, Digital volume correlation: Review of progress and challenges, *Exp. Mech.* 58 (2018) 661–708, <https://doi.org/10.1007/s11340-018-0390-7>.
- [29] S. Roux, F. Hild, P. Viot, D. Bernard, Three-dimensional image correlation from X-ray computed tomography of solid foam, *Compos. Part A – Appl. S.* 39 (2008) 1253–1265, <https://doi.org/10.1016/j.compositesa.2007.11.011>.
- [30] A. Benoit, S. Guerard, B. Gillet, G. Guillot, F. Hild, D. Mitton, J.-N. Perie, S. Roux, 3D analysis from micro-MRI during in situ compression on cancellous bone, *J. Biomech.* 42 (2009) 2381–2386, <https://doi.org/10.1016/j.jbiomech.2009.06.034>.
- [31] K. Madi, G. Tozzi, Q.H. Zhang, J. Tong, A. Cossey, A. Au, D. Hollis, F. Hild, Computation of full-field displacements in a scaffold implant using digital volume correlation and finite element analysis, *Med. Eng. Phys.* 35 (2013) 1298–1312, <https://doi.org/10.1016/j.medengphy.2013.02.001>.
- [32] E. Dall'Ara, D. Barber, M. Viceconti, About the inevitable compromise between spatial resolution and accuracy of strain measurement for bone tissue: A 3D zero-strain study, *J. Biomech.* 47 (2014) 2956–2963, <https://doi.org/10.1016/j.jbiomech.2014.07.019>.
- [33] F. Comini, M. Palanca, L. Cristofolini, E. Dall'Ara, Uncertainties of synchrotron microCT-based digital volume correlation bone strain measurements under simulated deformation, *J. Biomech.* 86 (2019) 232–237, <https://doi.org/10.1016/j.jbiomech.2019.01.041>.
- [34] F. Gillard, R. Boardman, M. Mavrogordato, D. Hollis, I. Sinclair, F. Pierron, M. Browne, The application of digital volume correlation (DVC) to study the microstructural behaviour of trabecular bone during compression, *J. Mech. Behav. Biomed. Mater.* 29 (2014) 480–499, <https://doi.org/10.1016/j.jmbbm.2013.09.014>.
- [35] D. Liu, B. Gludovatz, H.S. Barnard, M. Kuball, R.O. Ritchie, Damage tolerance of nuclear graphite at elevated temperatures, *Nat. Commun.* 8 (2017) 1–9, <https://doi.org/10.1038/ncomms15942>.
- [36] E. Schöberl, C. Breite, A. Melnikov, Y. Swolfs, M.N. Mavrogordato, I. Sinclair, Fibre-direction strain measurements in a composite ply under quasi-static tensile loading using Digital Volume Correlation and in situ Synchrotron Radiation Computed Tomography, *Compos. Part A – Appl. S.* 137 (2020) 105935. <http://dx.doi.org/10.1016/j.compositesa.2020.105935>.
- [37] C. Paraskevoulakos, J.P. Forna-Kreutzer, K.R. Hallam, C.P. Jones, T.B. Scott, C. Gausse, D.J. Bailey, C.A. Simpson, D. Liu, C. Reinhard, C.L. Corkhill, M. Mostafavi, Investigating the microstructure and mechanical behaviour of simulant “lava-like” fuel containing materials from the Chernobyl reactor unit 4 meltdown, *Mater. Design* 201 (2021), <https://doi.org/10.1016/j.matdes.2021.109502>.
- [38] V. Mazars, O. Caty, G. Couegnat, A. Bouterf, S. Roux, S. Denneulin, J. Pailhes, G.L. Vignoles, Damage investigation and modelling of 3D woven ceramic matrix composites from X-ray tomography in-situ tensile tests, *Acta Mater.* 140 (2017) 130–139, <https://doi.org/10.1016/j.actamat.2017.08.034>.
- [39] L. Saucedo-Mora, T. Lowe, S. Zhao, P.D. Lee, P.M. Mummery, T.J. Marrow, In situ observation of mechanical damage within a SiC–SiC ceramic matrix composite, *J. Nucl. Mater.* 481 (2016) 13–23, <https://doi.org/10.1016/j.jnucmat.2016.09.007>.
- [40] T.J. Pirzada, D. Liu, J. Ell, H. Barnard, I. Šulák, M. Galano, T.J. Marrow, R.O. Ritchie, In situ observation of the deformation and fracture of an alumina-alumina ceramic-matrix composite at elevated temperature using x-ray computed tomography, *J. Eur. Ceram. Soc.* 41 (7) (2021) 4217–4230, <https://doi.org/10.1016/j.jeurceramsoc.2021.01.030>.
- [41] A. Haboub, H.A. Bale, J.R. Nasiatka, B.N. Cox, D.B. Marshall, R.O. Ritchie, A.A. MacDowell, Tensile testing of materials at high temperature above 1700 °C with in situ synchrotron X-ray micro-tomography, *Rev. Sci. Instrum.* 85 (2014), <https://doi.org/10.1063/1.4892437> 083702.
- [42] ASTM Standard C1341-13, Standard Test Method for Flexural Properties of Continuous Fiber-Reinforced Advanced Ceramic Composites, ASTM International, West Conshohocken, PA, 2018. <http://dx.doi.org/10.1520/C1341-13R18>.
- [43] T. Ferreira, W. Rasband, ImageJ User Guide IJ 1.46r, 2012.
- [44] Thermo ScientificTM AvizoTM Software 9, User's Guide, 2018.
- [45] T.J. Lu, Crack branching in all-oxide ceramic composites, *J. Am. Ceram. Soc.* 79 (1) (1996) 266–274, <https://doi.org/10.1111/j.1151-2916.1996.tb07908.x>.